ARTICLE

Check for updates

Continuous heralding control of vortex beams using quantum metasurface

Hong Liang [1,3], Hammad Ahmed[2,3], Wing Yim Tam[1], Xianzhong Chen [2✉] & Jensen Li [1✉]

Metasurfaces utilize engineered nanostructures to achieve control on all possible dimensions of light, encouraging versatile applications, including beam steering, multifunctional lensing, and multiplexed holograms. Towards the quantum optical regime for metasurfaces, although significant efforts have been put into generating and analyzing specific quantum states, control schemes to further manipulate these quantum states or information are still limited. Here, based on a metasurface, we propose and experimentally demonstrate a continuous heralding scheme to remotely control a vortex beam with high robustness to noise using polarization-entangled photon pairs. Our metasurface entangles polarization and orbital angular momentum (OAM) and the polarization selection on heralding photon erases the which-OAM information on signal photon. It induces an interference of two different OAM states remotely, manifesting a continuous orbital rotation. Our results show that meta-surfaces have potential applications in quantum communication and information processing in entangling information with increasing complexity in the content.

[1] Department of Physics, The Hong Kong University of Science and Technology, Clear Water Bay, 999077 Kowloon, Hong Kong, P. R. China. [2] School of Engineering and Physical Sciences, Heriot-Watt University, Edinburgh EH144AS, UK. [3] These authors contributed equally: Hong Liang, Hammad Ahmed. ✉email: x.chen@hw.ac.uk; jensenli@ust.hk

Metasurfaces, with a thin layer of subwavelength structures, have the distinct capability to control wavefront in high resolutions, thus enabling various applications such as anomalous beam steering, multifunctional lensing, vortex beam structuring, and multiplexed holograms generation[1–6]. These demonstrations show that metasurfaces can manipulate and hybridize nearly all degrees of freedom of light, including amplitude, phase, polarization, diffraction order, and orbital angular momentum (OAM). Specifically, structured beams with tailor-made profiles of both OAM and polarizations can now be generated using metasurfaces through spin–orbit interactions (SOI)[7–11]. Various metasurfaces have been proposed for the generation and manipulation of OAM beams. Examples include varying OAM along the propagation direction, composite vortex beams with multiple singularities, and asymmetric OAM distribution in multiple channels[12–14]. The generated beams, carrying different OAMs, have a great potential to enhance the channel capacity in optical communication, leading to applications like OAM-encoded holograms[15–19]. Recently, there have been tremendous efforts to extend the functionalities of metasurfaces into the quantum optical regime[20–23]. For example, metasurfaces can be used to construct high-dimensional quantum sources, manipulating and reconstructing quantum entangled states[24–26]. Metasurfaces also enable exotic effects in optical quantum interference, such as the control from destructive to constructive quantum interference or the elimination of certain states using quantum interference[27,28]. The multiple functionalities of metasurfaces induce quantum entanglements between spin and OAM or spin and diffraction order of the incident photons[29,30]. The tailor-made multichannel control of metasurfaces can further enhance the parallelism of quantum optical operations. It adds extra layers in expressing the photon states and thus can enrich the mechanisms for quantum imaging and quantum communications[31–35].

In this work, we propose and experimentally demonstrate a continuous-heralding scheme in tuning the vortex beam generated from a metasurface with polarization-entangled photon pairs. As we shall see, enabled by a geometric-phase metasurface with tailor-made SOI to induce OAM interference and polarization entanglement between the photon pair (heralding and signal photon), we can select the heralding polarization to control the vortex structure of the signal photons remotely and continuously. Our work shows that metasurface can also be applied in the quantum optical regime for OAM control, including a nonlocal control on photons' vortex states utilizing the quantum state manipulation empowered by metasurfaces. Once we have such an ability, we can utilize metasurfaces for quantum encryption and communication with enhanced degrees of freedom. Such control may enable future developments of quantum communication protocols. We believe that our approach using metasurface can also be extended to more sophisticated vortex structures of the signal photon and opens a new avenue for quantum communication with increased information capacity.

Results and discussion

Continuous-heralding scheme. The proposed continuous-heralding scheme with a polarization-entangled photon pair (signal and heralding photons) is shown in Fig. 1a. The signal photon is sent to interact with the metasurface with SOI, while the heralding photon is sent to a polarization analyzer. The metasurface enables the entanglement between polarization and the OAM of the signal photon. Together with the polarization entanglement between the heralding and the signal photon, the polarization of the heralding photon and the vortex structure of the signal photon is entangled as a result. Thus, the heralding
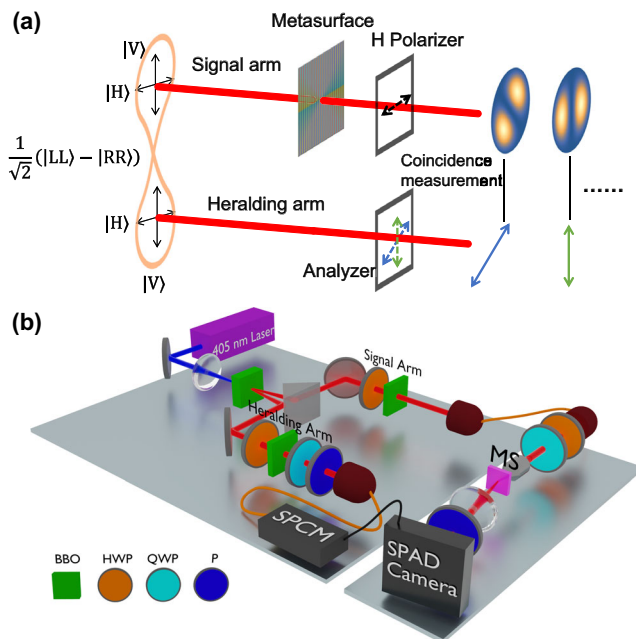

Fig. 1 Remote control on the vortex beam structure. a Schematic of the remote control. The signal photon of the polarization-entangled photon pair is sent to the metasurface to generate a polarization-dependent OAM state. The heralding photon is detected with selected polarization. The polarization selection of the heralding photon determines the vortex structure of the signal photon. **b** Experimental setup. The polarization-entangled photon pair is generated in the BBO type-II β-barium borate (BBO) crystal pumped by a 405 nm laser. The pair are separated by a prism into the heralding arm and signal arm. There are a half-wave plate (HWP) and BBO in each arm to compensate for the walk-off effects. The heralding photon would be polarization-selectively detected with a quarter-wave plate (QWP) and a polarizer (P) using a single-photon counting module (SPCM). The signal photon is sent to interact with the metasurface (MS) and imaged by a single-photon avalanche diode (SPAD) camera, which is gated by the heralding detection signal.

detection with a rotating linear polarization will result in a rotating vortex structure of the signal photons. The experimental implementation of the continuous heralding control scheme is shown in Fig. 1b. We generate the polarization-entangled photon pair by spontaneous parametric down-conversion (SPDC) with a 405 nm pump laser (beam in blue color) on a type-II β-barium borate (BBO) crystal. The generated photon pairs are split using a prism into heralding and signal arms (beams in red color). Each arm consists of a half-wave plate (HWP) with an optical axis at 45° with the horizontal axis and a BBO with half of the thickness of the main BBO to compensate for the translational and longitudinal walk-off effects[36]. The generated state can be expressed as $1/\sqrt{2}(|H\rangle_h|V\rangle_s + |V\rangle_h|H\rangle_s)$ with $|H\rangle$ ($|V\rangle$) and subscript h(s) denoting, respectively, the horizontal (vertical) polarization and the heralding (signal) photon. Through a long optical fiber, serving as a delay, the signal photon is sent to interact with the metasurface, with a HWP and a quarter-wave plate (QWP) placed before the metasurface to correct the polarization change from the long fiber. After the correction, the photon pairs are in the original state and can be rewritten as

$$|\psi\rangle = \frac{1}{\sqrt{2}}\left(|L\rangle_h|L\rangle_s - |R\rangle_h|R\rangle_s\right), \qquad (1)$$

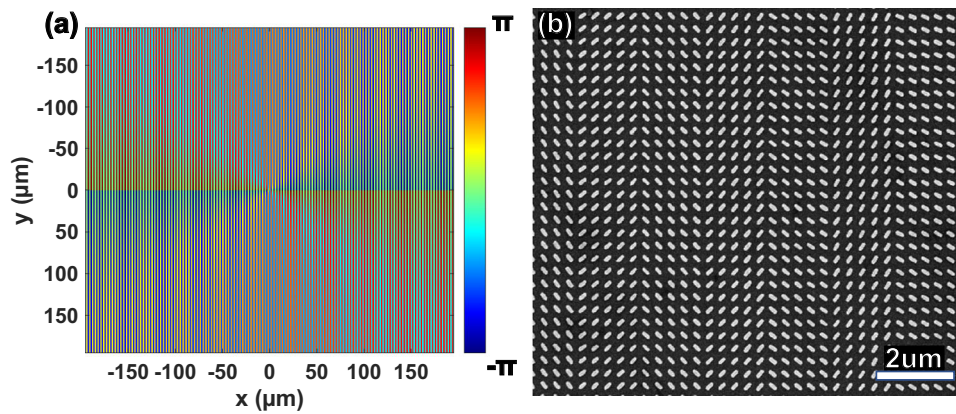where the $|L\rangle$ ($|R\rangle$) stands for left (right)-handed circular polarization (LCP/RCP).

Fig. 2 Metasurface design. a The phase profile of the metasurface for generating two off-axis optical vortex beams showing both phase gradients in the azimuthal direction and phase variations in the horizontal direction. **b** SEM image of the fabricated metasurface consisting of planar Au nanorods. The sample has a dimension of 390 μm × 390 μm. Each unicell has a size of 300 nm × 300 nm and consists of a nanorod.

The metasurface is designed to introduce a change in the OAM of the input light by $\Delta l = \pm 1$ ($+1$ for $|L\rangle$ and -1 for $|R\rangle$ polarization) and spin flipping of $|L\rangle \leftrightarrow |R\rangle$. Such an action has to occur at the same exit beam direction with a tailor-made SOI profile on metasurface. Here, we use the operator $\hat{M} = |R, +1\rangle_s \langle L|_s + |L, -1\rangle_s \langle R|_s$ to denote such an action of the metasurface. Then the signal photon after interacting with the metasurface is transformed to a state of

$$|\varphi\rangle = \hat{M}|\psi\rangle = \frac{1}{\sqrt{2}}(|L\rangle_h |R, +1\rangle_s - |R\rangle_h |L, -1\rangle_s) \qquad (2)$$

where the number ± 1 indicates the OAM of the signal photon. To enable the remote control of the vortex structure of the signal photon, we choose the state of the heralding photon as $|\phi\rangle_h = (|L\rangle_h + e^{i\phi_h}|R\rangle_h)/\sqrt{2}$, i.e., by a linear polarizer at an angle $\phi_h/2$ with the horizontal axis. Then the quantum entangled state collapses to

$$|\phi\rangle_s = {}_h\langle\phi|\varphi\rangle = \frac{1}{2}(|R, +1\rangle_s - e^{-i\phi_h}|L, -1\rangle_s), \qquad (3)$$

indicating that the signal photon is in a vector state determined by the polarization detection of the heralding photon. This state comprises tensor products of polarization states and OAM states, illustrated as a form of non-separable vector modes. To further reveal the vortex structure of the signal photon, we project the photon onto the horizontal polarization to retrieve the interference lobes, resulting in the final vortex state given by

$$|\phi\rangle_s \rightarrow \frac{1}{2\sqrt{2}}(|H, +1\rangle_s - e^{-i\phi_h}|H, -1\rangle_s) \qquad (4)$$

for different ϕ_h remotely controlled by the heralding polarization. The final signal photon is now a superposition of the two OAM states and will display as a rotating orbital in the intensity profile. Figure 1b shows the experimental setup for implementing our heralding scheme (see Supplementary Note 2). The heralding photon is projected to a certain polarization using a polarizer before being detected by the single photon counting module (SPCM). The output (electrical trigger) of SPCM is then used to herald the arrival of the corresponding signal photon on the single-photon avalanche diode (SPAD) camera to capture the interference patterns (between the two OAMs) of the signal photon as indicated by Eq. (4). We note that such a change of orbital shape (rotation of orbital in our case) caused by polarization can be interpreted as a form of spin Hall effect of light in the classical regime[9,37] either by performing two

experiments of orthogonal incident polarizations or by a superposition of incident polarizations. Promoting the spin Hall effect of light to the quantum optical regime by entangling with a heralding photon allows us to select any superpositions of the resulting orbitals by controlling the polarization state of the heralding photon.

Metasurface design with OAM interference. The proposed scheme requires the output beam with opposite OAMs exiting in the same direction for interference, which can be achieved with a geometric-phase metasurface combining a q-plate and a beam splitter. The geometric (Pancharatnam-Berry) phase distribution, as shown in Fig. 2a, is governed by

$$\phi(x, y) = \arg\left(E_1 e^{i\left(l\theta + \frac{\Delta\phi_{off}}{p}x\right)} + E_2 e^{i\left(l\theta - \frac{\Delta\phi_{off}}{p}x\right)}\right). \qquad (5)$$

where the two terms (with amplitudes $E_1 = E_2$ for convenience) correspond to the two transmitted split beams. Here, $l = \Delta l = 1$ is the topological charge of the metasurface to induce the OAM change Δl of the input LCP beam. $\theta = \arctan(y/x)$ is the azimuthal angle, and $\Delta\phi_{off} = \pi/5$ is the phase difference between neighboring unit cells with a period $p = 300$ nm, which introduces phase gradient in the horizontal direction and thus deflection of the input light. It is worth noting that the off-axis deflecting angles of the two exit beams are chosen to have the same magnitude but opposite signs to avoid the residue beam exiting in the normal direction (the non-converted part of the incident beam). To experimentally realize the design, a plasmonic metasurface (390 μm × 390 μm) consisting of planar gold nanorods (200 nm long, 80 nm wide, and 40 nm thick) with spatially varying orientations is fabricated on an ITO-coated glass substrate using the standard electron beam lithography (see Supplementary Note 1). The geometry of the nanorod is based on our previous work and has a polarization conversion efficiency of 13% at 810 nm[38]. To obtain the geometric phase of the output beam, the orientation angles of the nanorods are set to be half of the phase angles of the phase profile[9]. A scanning electron microscopy (SEM) image of the fabricated sample is shown in Fig. 2b.

To verify the OAM interference of the metasurface first in the classical regime, a supercontinuum laser (NKT Photonics SuperK EXTREME) is used as the light source at normal incidence on the metasurface with a selected wavelength at 650 nm. A linear polarizer and a QWP are used to control the incident polarization state. The intensity profiles of the generated optical vortex beams are projected on a screen and then captured by an iPhone camera,
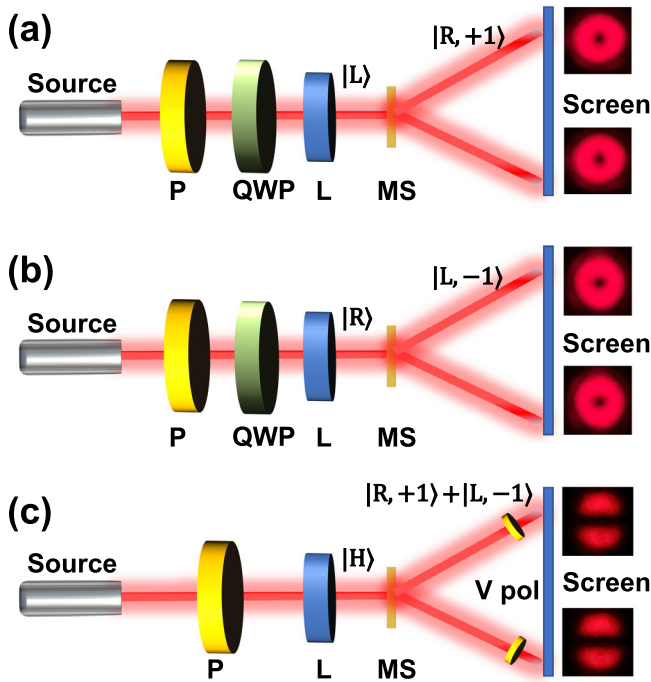
Fig. 3 OAM interference. a The input light is prepared to be left circularly polarized (LCP, $|L\rangle$) using a polarizer (P) and a quarter-wave plate (QWP) and focused onto the metasurface (MS) with a lens (L). The deflected light forms a pair of right circularly polarized (RCP, $|R\rangle$) vortex beams at angles of $\pm 12.5°$ with $l = 1$. **b** Upon the illumination of a pure RCP light beam, the deflected light forms a pair of LCP vortex beams at angles of $\pm 12.5°$ with $l = -1$. **c** When the input light is horizontally polarized ($|H\rangle$), the resultant beam in either exit direction is a superposition of RCP and LCP beams with opposite OAMs. The vortex structure is diagnosed with a vertical (V) polarizer. Insets show the transmitted intensity patterns captured at 650 nm.

as shown in Fig. 3 for the schematic experimental setup. Upon the illumination of LCP light, a pair of off-axis RCP centrosymmetric vortex beams with $l = +1$ are simultaneously generated at angles $+12.5°$ and $-12.5°$ (as illustrated in Fig. 3a). By switching the helicity of incident light to RCP, the propagating directions of two generated vortex beams are swapped with respect to the axis of incident light. Meanwhile, the sign of OAM is also flipped, i.e., $l = -1$ as the sign of the phase change introduced by the metasurface is dependent on the helicity of circular polarization (Fig. 3b)[39]. As a result, the intensity shows up as a doughnut-shaped profile since there is a phase singularity at the center of each beam. A horizontally polarized light, which can be decomposed into the superposition of two circularly polarized beams with opposite helicities, after interacting with the metasurface, can be described as

$$\hat{M}|H\rangle = \hat{M}\frac{1}{\sqrt{2}}(|L\rangle + |R\rangle) = \frac{1}{\sqrt{2}}(|R, +1\rangle + |L, -1\rangle).$$

The superposition state can be evaluated with a polarizer, as illustrated in Fig. 3c. The Jones matrix of the polarizer with a transmission axis making an angle α with the horizontal axis can be expressed as $\hat{P}(\alpha) = (\cos\alpha|H\rangle + \sin\alpha|V\rangle)(\cos\alpha\langle H| + \sin\alpha\langle V|)$[40]. Thus, the transmitted intensity profile can be obtained by $\langle H|\hat{M}^\dagger \hat{P}(\alpha)\hat{M}|H\rangle = 2\cos^2(\theta + \alpha)$, leading to two lobes in θ, the azimuthal direction of the beam, where we have used $|l\rangle = e^{il\theta}$. For

the current case, we choose $\alpha = \pi/2$ (vertical polarizer), and thus the lobes exhibit maximum intensity at $-90°$ and $90°$, as shown in Fig. 3c. In essence, the metasurface design guarantees that the two generated OAM beams, $l = \pm 1$, overlap and interfere with each other for any linearly polarized incident light.

Demonstration of orbital rotation with heralding control. Figure 4 shows the experimental and theoretical results, corresponding to the experimental setup in Fig. 1b. In the experiment, we use polarization-entangled photon pairs at 810 nm. Only one arm of the deflected vortex signal beams (at 15.7°) is imaged on the SPAD camera. The heralding photons, once detected, are used to trigger the imaging of the corresponding signal photons by the SPAD camera. 6000 images of 100-ms-long and 8-bit resolution are captured with background white noise subtracted for each configuration to enhance the signal-to-noise ratio (see Supplementary Note 2 for details). Here we use a polarizer, with a tunable polarization angle, in the heralding arm to conduct remote and continuous control of the vortex structure of the signal photons. For demonstration purposes, the results of the vortex structure for selected heralding polarizations, from the horizontal, diagonal, vertical, to antidiagonal, are shown in Fig. 4a–d, corresponding to changing ϕ_h from 0, $\pi/2, \pi$, to $3\pi/2$, where $\phi_h/2$ is the linear polarization angle with respect to the horizontal axis. Then Eq. (4) above can be rewritten as $|+1\rangle + e^{i(\pi-\phi_h)}|-1\rangle$ with polarization notation and normalization factor omitted for convenience, leading to an intensity profile of $|e^{i\theta} + e^{i(\pi-\phi_h)}e^{-i\theta}|^2 \propto \sin^2(\theta + \phi_h/2)$, where θ is the azimuthal angle of the beam profile. Thus, the final interference pattern exhibits rotating lobes with orientations dependent on the polarization angle $\phi_h/2$. The maximum and minimum intensities appear, respectively, at $\theta_{max} = (n + 1/2)\pi - \phi_h/2$ and $\theta_{min} = n\pi - \phi_h/2$ for $n = 0, 1$.

For example, Fig. 4a shows the interference pattern captured for the heralding photons of horizontal (H) polarization. In this case, the vortex state of the signal photons collapses to $|+1\rangle - |-1\rangle$, of which the intensity drops down to zero for $\theta = 0$ or π, resulting in a profile of two (bright) lobes with a horizontal dark line in between, as shown in Fig. 4a. On the other hand, using vertical (V) photons to herald, we get the result shown in Fig. 4c, which is from the state $|+1\rangle + |-1\rangle$. This vortex state shows up as two lobes and a vertical dark line in between. Similarly, the results with diagonal (D) and antidiagonal (A) heralding photons are shown in Fig. 4b, d with vortex states $|+1\rangle \pm i|-1\rangle$ where the "+" ("−") sign is for the $D(A)$ polarization. The experimental results align well with the theory results (insets) except for a global shift of around 8° in the anticlockwise direction due to small deviations in the orientations of the sample and the polarizers. When the heralding linear polarization rotates stepwise from $|H\rangle, |D\rangle, |V\rangle$, to $|A\rangle$, the orbital image of the signal photons rotates 45° for each step in the clockwise direction. In fact, with the interference profile dictated as $\sin^2(\theta + \phi_h/2)$, continuous change in the heralding linear polarization angle ($\phi_h/2$) induces the orbital image of the signal photons to rotate clockwise with the same angle change via entanglement. The heralding scheme can be extended to include circular polarizations, LCP or RCP, by adding a QWP in the heralding arm to probe the $|+1\rangle$ or the $|-1\rangle$ state of the signal photon, producing a doughnut-shaped orbital image as shown in Supplementary Fig. S2a, b (see Supplementary Note 3). On the other hand, we can also obtain a doughnut-shaped orbital image by adding heralded images from orthogonal polarizations, e.g., adding Fig. 4a and c, or adding Fig. 4b and d, as shown in Supplementary Fig. S1d, e, which is similar to the single-photon
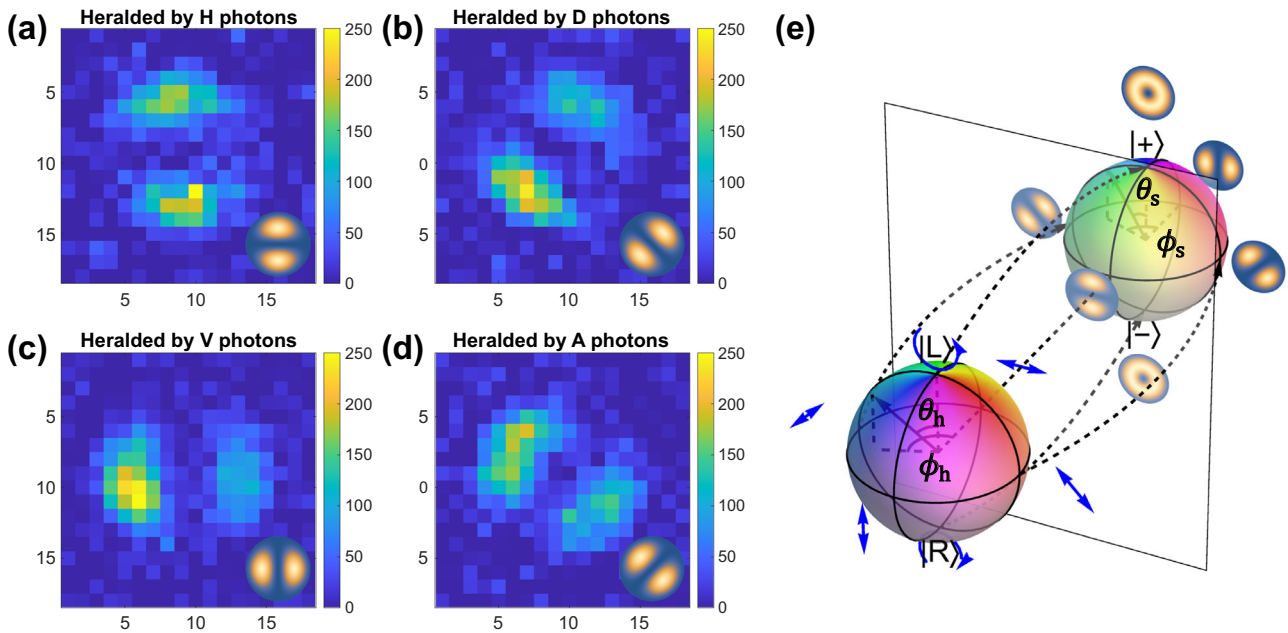
Fig. 4 Heralded images of signal vortex states shown as rotating orbitals for different heralding polarizations. a–d Results with heralding polarization of $|H\rangle$, $|D\rangle$, $|V\rangle$, and $|A\rangle$. Lower-right insets are the theoretical predictions. **e** Mapping between the two Poincaré spheres for the heralding polarization and signal vortex state. Points with the same color on the two spheres show matching pairs of the controlling polarization and corresponding vortex state. Specific example pairs are connected using dashed arrows.

intensity image without heralding mechanism (Supplementary Fig. S1c). This is because the single-photon image captures a mixed state of the signal photons, which can be evaluated by tracing out the density matrix corresponding to the output state given by Eq. (2) using two orthogonal polarizations of the heralding photon. The density matrix can be expressed before the horizontal polarizer in front of the SPAD camera as

$$\rho_s = \mathrm{Tr}_h\big[|\varphi\rangle\langle\varphi|\big] = \frac{1}{2}\big(|R,+1\rangle_s\langle R,+1|_s + |L,-1\rangle_s\langle L,-1|_s\big),$$

and after the horizontal polarizer as

$$\rho_s \rightarrow \frac{1}{4}|H,+1\rangle_s\langle H,+1|_s + \frac{1}{4}|H,-1\rangle_s\langle H,-1|_s. \quad (6)$$

On the other hand, adding images in Fig. 4a and c means a corresponding sum of density matrices

$$(|+1\rangle + |-1\rangle)(\langle+1| + \langle-1|) + (|+1\rangle - |-1\rangle)(\langle+1| - \langle-1|)$$
$$\propto |+1\rangle\langle+1| + |-1\rangle\langle-1|,$$

which exhibits the same image profile as the one given by Eq. (6). In other words, before heralding, the photon state is indeed a superposition of both imaging results heralded by photons of orthogonal polarizations. The heralding detection allows us to post-select any vortex state using the corresponding heralding polarization. This phenomenon can actually be understood as a quantum eraser[41,42]. Without heralding, the OAM path of the signal photon, compared to the spatial path in a conventional quantum eraser experiment, can be identified with the corresponding heralding polarization, while with a projection of the heralding polarization, the information regarding OAM path is erased and thus an interference between two OAM states shows up. Another aspect related to the heralding imaging technique is the robustness to noise[43]. In our measurement, the noise mainly comes from the environmental background noise and the electrical noise of the detectors. The heralding imaging works in a way that when one heralding photon gets detected, an electrical trigger is sent to the camera, and the camera exposes for only a short period of time. In other words, instead of taking

photos continuously, the camera only takes photos when there is a heralding detection signal. Compared with classical intensity imaging, this approach effectively reduces the exposure time, eliminating most of the environmental noise, and can potentially improve the SNR of the measurement, which is critical in some photon-hungry applications such as quantum biosensing, imaging, and secure communication[44–46]. Our heralded images (e.g., adding Fig. 4a and c) show an average signal-to-noise ratio (Pearson correlation coefficient) of 8.5 dB (0.90), while it is only up to 3.9 dB (0.71) without the heralding triggers, demonstrating well the robustness of the heralding approach (see Supplementary Note 4).

Now, we would like to discuss the meaning of our continuous heralding scheme as a generic mapping between heralding polarization and the vortex structure being remotely controlled. Suppose the heralding photon is projected by an arbitrary polarization analyzer, i.e., not necessarily just a polarizer but a combination of a QWP and a polarizer, to cover any arbitrary polarization state on the Poincaré sphere. In this case, we introduce an additional parameter θ_h into the polarized heralding detection as $|\phi\rangle_h = \cos(\theta_h/2)|L\rangle_h + e^{i\phi_h}\sin(\theta_h/2)|R\rangle_h$. Then, the signal photon, after interacting with the metasurface, becomes

$$|\phi\rangle_s = {}_h\langle\phi|\varphi\rangle = \frac{1}{\sqrt{2}}\left(\cos\left(\frac{\theta_h}{2}\right)|R,+1\rangle_s - \sin\left(\frac{\theta_h}{2}\right)e^{-i\phi_h}|L,-1\rangle_s\right). \quad (7)$$

Then the resultant vortex state in the exit beam after the horizontal polarizer can be expressed as

$$|\phi\rangle_s \rightarrow \frac{1}{2}\left(\cos\left(\frac{\theta_h}{2}\right)|H,+1\rangle_s - \sin\left(\frac{\theta_h}{2}\right)e^{-i\phi_h}|H,-1\rangle_s\right). \quad (8)$$

In fact, θ_h and ϕ_h denote the polar and azimuthal angles on the polarization Poincaré sphere for the heralding photon polarization. The resultant signal photon vortex state given by Eq. (8), in turn, lives in a higher-order Poincaré sphere[47–49]. Thus, the relationship between the heralding photon and the signal vortex state can be visualized in Fig. 4e. Points (θ_h, ϕ_h) on the

polarization Poincaré sphere, denoted in different colors, describe all possible heralding polarization states. According to Eq. (8), the controlled vortex state of the signal photon, a combination of two orthogonal OAM modes ($|+1\rangle$ and $|-1\rangle$), can also be described with a higher-order Poincaré sphere. Similarly, we can use (θ_s, ϕ_s) to denote the vortex state which, in our control scheme, is equal to $(\theta_h, \pi - \phi_h)$. Therefore, we can use a mirror located (the vertical frame in Fig. 4e) in between two spheres to denote this mapping. The points with the same color on the two spheres denote a pair of controlling polarization and controlled vortex states. Specific example pairs are highlighted using arrows to indicate the corresponding mapping. The experimental results reported above correspond to the cases located on the equator (Fig. 4a–d) and at the two poles (Supplementary Fig. S2a, b) of the two Poincaré spheres. On the equator, the signal orbital orientation is controlled by the angle of the heralding linear polarization in a continuous manner. Based on the results, any intermediate states between the poles and the equator can also be achieved using elliptical heralding polarizations. However, one should note that, in our experiment, the efficiency can be further improved by using a dielectric metasurface that can simultaneously combine geometric and propagation phases[50,51]. Such a design can independently generate arbitrary phase profiles for the two orthogonal spins and hence the same and only one output direction for the two OAM states, which could potentially enhance the SNR or reduce the number of time frames required in the experiment. Furthermore, the current scheme can be extended to higher dimensions (e.g., other OAM values) or with other degrees of freedom, for example, path or holograms, indicating more sophisticated applications in quantum communications and information processing[52,53].

Conclusion

In conclusion, based on a geometric-phase metasurface, we experimentally demonstrate a heralding scheme, with great robustness of noise, to control vortex structures of OAM interference remotely and continuously using polarization-entangled photon pairs. Through this work, multifunctional metasurfaces further extend their applications in the quantum optical regime, providing a platform to implement quantum information processing with tailor-made vortex structures or to develop more sophisticated quantum eraser experiments. Importantly, such a continuous heralding control of rotating orbitals provides additional dimensions in the quantum state manipulation that could benefit future quantum communication protocols. With more complex metasurfaces, further extensions to higher OAM values, structured beams, and other degrees of freedom of light will be possible in enhancing the associated information capacity in quantum communication.

Methods

Sample fabrication. The geometric-phase metasurface consists of planar gold nanorods with spatially variant orientations sitting on an ITO-coated glass substrate. First, the substrate is cleaned with acetone for 10 min in an ultrasonic bath, followed by isopropyl alcohol (IPA) for 10 min. Then, a photoresist poly (methyl methacrylate) (PMMA) 950 A2 resist is spin-coated on the substrate at 1000 rpm for 60 s, producing a 100 nm-thick film. After that, the sample is baked on a hotplate at 180 °C for 5 min. Electron beam lithography (Raith PIONEER, 30 kV) is used to direct-write the nanorod pattern, which is then developed in MIBK:IPA (1:3) for 45 s and rinsed IPA for 45 s. Then an electron beam evaporator is used to deposit a 40 nm-thick gold film on the sample. Finally, the metasurface is ready for characterization after a lift-off process.

Quantum optical measurement. In the experiment, we use a 2-mm-thick type-II BBO and a 200 mW 405 nm laser (CrystaLaser DL-405-400) to generate the polarization-entangled photon pairs in a state of $1/\sqrt{2}(|HV\rangle + |VH\rangle)$, with a fidelity of 91.2% and a Bell parameter of 2.54 > 2 (see Supplementary Note 6). The half-opening angle of the generated photon pairs is designed to be 3°. The photons

are split into the signal arm and heralding arm using a prism. The photons in the heralding arm are detected with polarization selection using a single photon counting module (SPCM) (Excelitas-SPCM-800-14-FC), and the detection signals are sent to herald signal photons' arrival on the SPAD camera. Meanwhile, the signal photons are sent through a 10-m-long single-mode fiber to the imaging setup. A lens (focal length 100 mm) and a ×10 objective are used to focus the signal beam onto the metasurface. The vortex beam generated from the metasurface is imaged by the SPAD camera (SPAD512S) using a lens with a focal length of 45 mm. The heralded image of the signal photons in Fig. 4a–d are all retrieved using 6000 frames with external triggers from SPCM and with background white noise subtracted. The background is measured using the same triggering setting with blocked signal photons. Each time frame spans 100 ms with a maximum of 255 photon counts in each pixel. Each trigger from the SPCM would turn on the camera for a detection window of 10 ns. With heralding photon counting rate up to 300 kHz, there would be multiple triggers in one frame, and the detection events in each triggered window would accumulate into one frame. The polarization conversion efficiency of the gold nanostructure is around 13% at 810 nm, and other information related to the experimental efficiency is in Supplementary Note 5.

References
1. Yu, N. et al. Light propagation with phase discontinuities: generalized laws of reflection and refraction. *Science* **334**, 333 (2011).
2. Khorasaninejad, M. et al. Metalenses at visible wavelengths: diffraction-limited focusing and subwavelength resolution imaging. *Science* **352**, 1190 (2016).
3. Yue, F. et al. Vector vortex beam generation with a single plasmonic metasurface. *ACS Photonics* **3**, 1558 (2016).
4. Zheng, G. et al. Metasurface holograms reaching 80% efficiency. *Nat. Nanotechnol.* **10**, 4 (2015).
5. Chen, H.-T., Taylor, A. J. & Yu, N. A review of metasurfaces: physics and applications. *Rep. Prog. Phys.* **79**, 076401 (2016).
6. Qiu, C.-W., Zhang, T., Hu, G. & Kivshar, Y. Quo Vadis, metasurfaces? *Nano Lett.* **21**, 5461 (2021).
7. Maguid, E. et al. Photonic spin-controlled multifunctional shared-aperture antenna array. *Science* **352**, 1202 (2016).
8. Bliokh, K. Y., Rodríguez-Fortuño, F. J., Nori, F. & Zayats, A. V. Spin–orbit interactions of light. *Nat. Photon* **9**, 12 (2015).
9. Li, G. et al. Spin-enabled plasmonic metasurfaces for manipulating orbital angular momentum of light. *Nano Lett.* **13**, 4148 (2013).
10. Leung, H. M. et al. Exceptional point-based plasmonic metasurfaces for vortex beam generation. *Opt. Express* **28**, 503 (2020).
11. Bao, Y., Ni, J. & Qiu, C.-W. A minimalist single-layer metasurface for arbitrary and full control of vector vortex beams. *Adv. Mater.* **32**, 1905659 (2020).
12. Dorrah, A. H., Rubin, N. A., Tamagnone, M., Zaidi, A. & Capasso, F. Structuring total angular momentum of light along the propagation direction with polarization-controlled meta-optics. *Nat. Commun.* **12**, 1 (2021).
13. Ming, Y. et al. Creating composite vortex beams with a single geometric metasurface. *Adv. Mater.* **34**, 2109714 (2022).
14. Ahmed, H. et al. Multichannel superposition of grafted perfect vortex beams. *Adv. Mater.* **34**, 2203044 (2022).
15. Ren, H. et al. Metasurface orbital angular momentum holography. *Nat. Commun.* **10**, 2986 (2019).
16. Ren, H. et al. Complex-amplitude metasurface-based orbital angular momentum holography in momentum space. *Nat. Nanotechnol.* **15**, 948 (2020).
17. Nagali, E. et al. Quantum information transfer from spin to orbital angular momentum of photons. *Phys. Rev. Lett.* **103**, 013601 (2009).
18. Liu, M. et al. Broadband generation of perfect poincaré beams via dielectric spin-multiplexed metasurface. *Nat. Commun.* **12**, 1 (2021).
19. Chen, S. et al. Cylindrical vector beam multiplexer/demultiplexer using off-axis polarization control. *Light Sci. Appl.* **10**, 1 (2021).
20. Solntsev, A. S., Agarwal, G. S. & Kivshar, Y. S. Metasurfaces for quantum photonics. *Nat. Photonics* **15**, 5 (2021).
21. Fan, Y., Liang, H., Li, J., Tsai, D. P. & Zhang, S. Emerging trend in unconventional metasurfaces: from nonlinear, non-hermitian to nonclassical metasurfaces. *ACS Photonics* **9**, 2872 (2022).

22. Kort-Kamp, W. J. M., Azad, A. K. & Dalvit, D. A. R. Space–time quantum metasurfaces. *Phys. Rev. Lett.* **127**, 043603 (2021).

23. Jha, P. K., Ni, X., Wu, C., Wang, Y. & Zhang, X. Metasurface-enabled remote quantum interference. *Phys. Rev. Lett.* **115**, 025501 (2015).

24. Li, L. et al. Metalens-array–based high-dimensional and multiphoton quantum source. *Science* **368**, 1487 (2020).

25. Wang, K. et al. Quantum metasurface for multiphoton interference and state reconstruction. *Science* **361**, 1104 (2018).

26. Gao, Z. Su, Q., Song, P. & Genevet, K. E. Dorfman, Metasurface for complete measurement of polarization Bell state. *Nanophotonics* **12**, 569 (2022).

27. Li, Q. et al. A non-unitary metasurface enables continuous control of quantum photon–photon interactions from bosonic to fermionic. *Nat. Photonics* **15**, 267–271 (2021).

28. Liang, H. et al. One-sided destructive quantum interference from an exceptional-point-based metasurface. *Phys. Rev. A* **104**, 063710 (2021).

29. Stav, T. et al. Quantum entanglement of the spin and orbital angular momentum of photons using metamaterials. *Science* **361**, 1101 (2018).

30. Georgi, P. et al. Metasurface interferometry toward quantum sensors. *Light Sci. Appl.* **8**, 1 (2019).

31. Gao, Y.-J. et al. Multichannel distribution and transformation of entangled photons with dielectric metasurfaces. *Phys. Rev. Lett.* **129**, 023601 (2022).

32. Yung, T. K., Liang, H., Xi, J., Tam, W. Y. & Li, J. Jones-matrix imaging based on two-photon interference. *Nanophotonics* **12**, 579 (2022).

33. Altuzarra, C. et al. Imaging of polarization-sensitive metasurfaces with quantum entanglement. *Phys. Rev. A* **99**, 020101 (2019).

34. Vega, A., Pertsch, T., Setzpfandt, F. & Sukhorukov, A. A. Metasurface-assisted quantum ghost discrimination of polarization objects. *Phys. Rev. Appl.* **16**, 064032 (2021).

35. Zhou, J. et al. Metasurface enabled quantum edge detection. *Sci. Adv.* **6**, eabc4385 (2020).

36. Kwiat, P. G. et al. New high-intensity source of polarization-entangled photon pairs. *Phys. Rev. Lett.* **75**, 4337 (1995).

37. Leary, C. C., Raymer, M. G. & van Enk, S. J. Spin and orbital rotation of electrons and photons via spin-orbit interaction. *Phys. Rev. A* **80**, 061804(R) (2009).

38. Wang, R. et al. Metalens for generating a customized vectorial focal curve. *Nano Lett.* **21**, 2081 (2021).

39. Yue, F. et al. Multichannel polarization-controllable superpositions of orbital angular momentum states. *Adv. Mater.* **29**, 1603838 (2017).

40. Ma, A., Intaravanne, Y., Han, J., Wang, R. & Chen, X. Polarization detection using light's orbital angular momentum. *Adv. Opt. Mater.* **8**, 2000484 (2020).

41. Walborn, S. P., Terra Cunha, M. O., Pádua, S. & Monken, C. H. Double-slit quantum eraser. *Phys. Rev. A* **65**, 033818 (2002).

42. Nape, I., Ndagano, B. & Forbes, A. Erasing the orbital angular momentum information of a photon. *Phys. Rev. A* **95**, 053859 (2017).

43. Morris, P. A., Aspden, R. S., Bell, J. E. C., Boyd, R. W. & Padgett, M. J. Imaging with a small number of photons. *Nat. Commun.* **6**, 5913 (2015).

44. Yepiz-Graciano, Pablo et al. Quantum optical coherence microscopy for bioimaging applications. *Phys. Rev. Appl.* **18**, 034060 (2022).

45. Liu, S.-K. et al. Real-time quantum edge enhanced imaging. *Opt. Express* **28**, 35415 (2020).

46. Cozzolino, D., Da Lio, B., Bacco, D. & Oxenløwe, L. K. High-dimensional quantum communication: benefits, progress, and future challenges. *Adv. Quantum Technol.* **2**, 1900038 (2019).

47. Milione, G., Sztul, H. I., Nolan, D. A. & Alfano, R. R. Higher-order Poincaré sphere, stokes parameters, and the angular momentum of light. *Phys. Rev. Lett.* **107**, 053601 (2011).

48. Forbes, A., de Oliveira, M. & Dennis, M. R. Structured light. *Nat. Photonics* **15**, 253 (2021).

49. Shen, Y., Wang, Z., Fu, X., Naidoo, D. & Forbes, A. SU(2) Poincaré sphere: a generalized representation for multidimensional structured light. *Phys. Rev. A* **102**, 031501 (2020).

50. Balthasar Mueller, J. P., Rubin, N. A., Devlin, R. C., Groever, B. & Capasso, F. Metasurface polarization optics: independent phase control of arbitrary orthogonal states of polarization. *Phys. Rev. Lett.* **118**, 113901 (2017).

51. Li, Z. et al. Three-channel metasurfaces for simultaneous meta-holography and meta-nanoprinting: a single-cell design approach. *Laser Photonics Rev.* **14**, 2000032 (2020).

52. Li, Z.-X. et al. High-dimensional entanglement generation based on a Pancharatnam–Berry phase metasurface. *Photon. Res.* **10**, 2702 (2022).

53. Erhard, M., Krenn, M. & Zeilinger, A. Advances in high-dimensional quantum entanglement. *Nat. Rev. Phys.* **2**, 7 (2020).

Acknowledgements

Author contributions

J.L. initiated the project. J.L. and H.L. conceived the idea. H.A. designed and fabricated the metasurface. H.L. conducted the experiment and analyzed the data. H.L. and H.A. wrote the manuscript, and J.L., X.C., and W.Y.T. revised the manuscript. J.L. and X.C. supervised the project.

Competing interests

The authors declare no competing interests.

Additional information

Supplementary information The online version contains supplementary material available at https://doi.org/10.1038/s42005-023-01262-5.

Correspondence and requests for materials should be addressed to Xianzhong Chen or Jensen Li.

Peer review information *Communications Physics* thanks the anonymous reviewers for their contribution to the peer review of this work.

Reprints and permission information is available at http://www.nature.com/reprints

Publisher's note Springer Nature remains neutral with regard to jurisdictional claims in published maps and institutional affiliations.